Theoretical studies of atomic structure and electronic structure in ternary amorphous Al - Cu - Y and Mg - Cu - Y alloys

Theoretical studies of atomic structure and electronic structure in ternary amorphous Al–Cu–Y and Mg–Cu–Y alloys

N Takeichi†, H Sato‡ and U Mizutani†

† Department of Crystalline Materials Science, Nagoya University, Furo-cho, Chikusa-ku, Nagoya 464-01, Japan
‡ Department of Physics, Aichi University of Education, Kariya-shi, Aichi-ken 448, Japan

Abstract. The atomic structure for the amorphous $Al_x(Cu_{0.4}Y_{0.6})_{100-x}$ and $Mg_x(Cu_{0.4}Y_{0.6})_{100-x}$ ($x = 30$ and 80) alloys has been calculated in molecular dynamics simulations with the use of the Hausleitner–Hafner approach for the construction of the interatomic potentials. The parameters are adjusted so as to reconcile the resulting radial distribution function (RDF) spectrum with the measured one as closely as possible. Using the atomic structure thus obtained, the valence band structure is calculated in the LMTO recursion method. We show in this way the development of different chemical bonding states, depending on whether the third element introduced into the amorphous Cu–Y matrix is Al or Mg, and can successfully explain the Al and Mg concentration dependence of various physical properties.

1. Introduction

Fukunaga *et al* [1] (hereafter referred to as I) revealed that the short-range order develops in an entirely different manner depending on whether Al or Mg atoms are introduced into the amorphous Cu–Y matrix and that various physical properties, including the crystallization temperature, the electronic specific heat coefficient and resistivity at 300 K, depend crucially on this short-range order. However, we realize that only averaged properties are measured for disordered systems such as liquid and amorphous alloys and that the coordinates of individual atoms cannot be uniquely determined. Nevertheless, the calculation of the band structure for amorphous alloys has been a pressing need in the last two decades, because the ever-increasing number of data on electronic properties requires a more detailed knowledge of the electronic structure for satisfactory interpretation.

A number of band calculations have been reported for the binary amorphous alloys in the literature. Fujiwara [2], for example, calculated the electron density of states for metal–metalloid amorphous alloys such as amorphous Fe–P and Fe–B alloys on the basis of the relaxed dense random packing model, which is constructed so as to reproduce the experimental radial distribution function. Once the atomic structure is constructed, the electronic energy eigenvalues are derived using the linear muffin-tin orbital (LMTO) method [3] in combination with the atomic sphere approximation (ASA) and the density of states is calculated by the recursion method [4].

Both the atomic structure and electronic structure of a large number of Y-based amorphous alloys have been calculated by Hausleitner *et al* [5], using the so-called

hybridized nearly-free-electron tight-binding bond (NFE TBB) approach developed by Hausleitner and Hafner [6]. The interatomic potentials are calculated within the framework of the NFE TBB approach and are employed in the molecular dynamics to construct the atomic structure of a given amorphous alloy. The electronic density of states is then calculated in the LMTO supercell calculations. The experimentally observed RDF spectra and photoemission spectra for amorphous Y–M (M = Zn, Cu, Ni, Fe and Mn) alloys were well reproduced by their calculations. In such realistic calculations, the observed atomic structure must be well reproduced in the computer. This is the reason why the theoretical calculations have been so far limited only to the binary amorphous alloys, to which detailed experimental data on the atomic structure are often available.

As discussed in I, ternary amorphous alloys are of particular interest, since observed physical properties often strongly depend on the third element added to a binary amorphous matrix. This unique behaviour in ternary amorphous alloys certainly originates from the formation of the different short-range order or the difference in the bonding strength between the two host elements in the matrix and the added third element. Indeed, both atomic and electronic structures in the ternary amorphous $Al_x(Cu_{0.4}Y_{0.6})_{100-x}$ and $Mg_x(Cu_{0.4}Y_{0.6})_{100-x}$ (they are hereafter abbreviated as $[Al]_x$ and $[Mg]_x$, respectively) alloys have been determined in I and the emphasis was laid on the finding that the third elements Al and Mg contribute to the formation of entirely different short-range orders and affect the band structure of the amorphous Cu–Y alloy in a different manner.

To the best of our knowledge, the construction of the atomic structure and the subsequent band calculations for the ternary amorphous alloys have not been attempted because of two main reasons: firstly, as mentioned above, experimental information about the atomic structure for the ternary amorphous alloys is very limited and, secondly, too many interatomic potentials have to be determined in the molecular dynamics modelling. Fortunately, the local atomic structures for both amorphous $[Al]_x$ and $[Mg]_x$ alloys with $x = 30$ and 80 have been experimentally well deduced. Though some ambiguity remains in the determination of many interatomic potentials, we have attempted in this calculation to construct the atomic structures for the ternary $[Al]_x$ and $[Mg]_x$ alloys with $x = 30$ and 80 so as to conform as much as possible to the experimentally derived RDF spectra. The valence band structures are then calculated in the recursion method using the atomic structure thus derived. A proper determination of the atomic structure can be confirmed by comparing the resulting band calculations with the observed photoemission and soft-x-ray emission spectra. Based on the band calculations, we interpret the Al and Mg concentration dependence of the observed electronic specific heat coefficient and resistivity at 300 K reported in I.

2. Calculation of interatomic potentials

The interatomic potentials in the present amorphous alloys have been constructed within the framework of the Hausleitner–Hafner approach [6]. The sp-electron contribution to the interatomic potential is calculated using the pseudopotential perturbation theory [7], whereas the d-electron contribution is given in the TBB formalism. The latter is divided into a repulsive term $V_R(R)$ due to the d-state orthogonality and an attractive term $V_B(R)$ due to the bond energy. For simplicity, only the nearest-neighbour atomic pair interactions on the Bethe lattice are taken into account. Furthermore, the total effective pair potential $V_{\alpha\beta}(R)$ for the atomic pair $\alpha\beta$ can be expressed simply as the sum of the sp- and d-electron contributions:

$$V_{\alpha\beta}(R) = V_{s,\alpha\beta}(R) + V_{d,\alpha\beta}(R) \tag{1}$$

where the sp-electron contribution $V_{s,\alpha\beta}(R)$ is given as

$$V_{s,\alpha\beta}(R) = \frac{2N_{s,\alpha}N_{s,\beta}}{R}\left(1 + 16\int_0^\infty \frac{\chi(q)}{\varepsilon(q)}\frac{\cos(qR_{c,\alpha})\cos(qR_{c,\beta})}{q^3}\sin(qR)\,\mathrm{d}q\right). \tag{2}$$

Here the second term in the bracket is expressed in terms of a local empty-core pseudopotential with the core radius $R_{c,\alpha}$ for the atomic species α, and the susceptibility $\chi(q)$ and dielectric function $\varepsilon(q)$ of the sp electron is given as a function of its average concentration. The sp- and d-electron contributions to the interatomic potential are calculated by using the measured density described in I. As is clear from the argument above, the sp–d hybridization effect is completely ignored in equation (1). Indeed, the importance of incorporating the p–d hybridization effect will be pointed out in section 3.2 in the construction of the pair potentials for the ternary amorphous $[Al]_x$ alloys.

As mentioned above, the d-electron contribution $V_{d,\alpha\beta}(R)$ in equation (1) consists of two terms:

$$V_{d,\alpha\beta}(R) = V_{B,\alpha\beta}(R) + V_{R,\alpha\beta}(R). \tag{3}$$

Here the first term representing an attractive bond potential for the atomic pair $\alpha\beta$ is given as

$$V_{B,\alpha\beta}(R) = \frac{4\sqrt{14W_\alpha W_\beta r_\alpha^5 r_\beta^5}}{R^5}\Theta_{\alpha\beta} \tag{4}$$

where W_α is the band width of the d band for the transition metal element α, r_α is the atomic radius for the element α and $\Theta_{\alpha\beta}$ is the bond order introduced in [6]. The second term representing the repulsive potential is expressed as

$$V_{R,\alpha\beta}(R) = \frac{8\sqrt{N_{d,\alpha}N_{d,\beta}}W_\alpha r_\alpha W_\beta r_\beta}{25}\left(\frac{\sqrt{r_\alpha r_\beta}}{R}\right)^8 \tag{5}$$

where $N_{d,\alpha}$ is the number of d electrons for the transition metal element α.

3. Calculations of the atomic structure

3.1. Amorphous $Cu_{40}Y_{60}$ alloy

It is well known that the local atomic structure of an amorphous phase reflects that of the crystalline phase existing at a composition close to that of the amorphous phase. There exists the CsCl-type CuY intermetallic compound in the Cu–Y phase diagram. Hence, our starting structure is built up by distributing randomly 800 Cu and 1200 Y atoms over the CsCl-type lattice sites. Furthermore, the periodic boundary condition is imposed. Molecular dynamics simulations are carried out to construct the atomic structure using equations (1)–(5). The system at the beginning is so unstable that every atom begins to move under the influence of interatomic potentials. Since the total energy is conserved, lowering of the potential energy inevitably increases the kinetic energy. A fourth-order prediction–correction algorithm with a time increment of $\Delta t = 10^{-15}$ s is employed for the integration of the Newtonian equation of motion. The atomic structure is frozen by quenching the system to room temperature in 5000 steps while keeping its volume constant. The quenching rate $\mathrm{d}T/\mathrm{d}t$ is found to be 10^{14} K s^{-1}.

As mentioned in the introduction, we consider it to be of vital importance to calculate an atomic structure very consistent with the experimentally derived one. According to the RDF spectrum shown in figure 4(a) in I, Cu atoms are preferentially bonded with Y atoms and distributed so as to avoid the formation of the Cu–Cu nearest-neighbour atomic

pair. However, we realized that a serious difficulty arose when the Cu and Y atomic radii employed by Hausleitner *et al* [5] were chosen. They assumed the respective atomic radii to be those in pure metals, i.e., $r_{Cu} = 1.41$ Å and $r_Y = 2.04$ Å, in their calculations for the amorphous $Cu_{35}Y_{65}$ alloy. The atomic structure was initially calculated in the present work using their atomic radii. However, we found that the Cu–Cu interatomic distance became shorter than the Cu–Y distance, in conflict with the experimental evidence mentioned above. Hausleitner *et al* apparently did not realize this difficulty and showed their calculated RDF spectrum without any comment.

To circumvent this difficulty, we directed our attention to the choice of Cu and Y atomic radii different from those in their elemental forms. A change in the atomic radius certainly affects both attractive and repulsive terms in equations (4) and (5) and its effect on the RDF spectrum would be reflected as a delicate interplay between these two. However, it is important to note that an increase in the Cu atomic radius contributes exclusively to increase the Cu–Cu repulsive term in equation (5), since the attractive term in equation (4) acting as the counterpart of equation (5) becomes extremely small for the Cu–Cu atom pair as a result of a vanishingly small bond order parameter for the Cu atom, having almost filled d states.

Since the CuY compound is used as a starting structure in the molecular dynamics simulations and the atomic radii of the Wigner–Seitz spheres in the compound are 1.71 Å for both the Cu and Y atoms, we consider the Cu–Cu distance to be increased by choosing these atomic radii. As expected, this certainly contributed to shift the Cu–Cu nearest-neighbour position to a large distance. Further adjustment is made to bring a better agreement with the experimentally derived RDF spectrum. The atomic radii of 1.80 Å for both Cu and Y atoms are finally chosen, as listed in table 1. The interatomic potentials thus obtained are shown in figure 1(a) and the RDF spectrum in figure 1(b). Now we see that not only is the minimum in the Cu–Cu potential shallowest and the farthest among three atomic pairs but also the positions of the Cu–Y and Y–Y atomic pairs in the calculated RDF spectrum could reproduce well the experimental spectrum.

Table 1. Input parameters for the calculation of interatomic potentials: number of s electrons $N_{s,\alpha}$, number of d electrons $N_{d,\alpha}$, core radius of s-electron pseudopotential $R_{c,\alpha}$, d-band width W_α, and d-electron energy level E_α.

	$\alpha = $ Al	$\alpha = $ Mg	$\alpha = $ Cu	$\alpha = $ Y
r_α (Å)	—	—	1.80	1.80
W_α (eV)	—	—	2.82	6.44
E_α (eV)	—	—	−6.91	−2.96
$N_{d,\alpha}$ (/atom)	—	—	9.56	1.69
$N_{s,\alpha}$ (/atom)	3.00	2.00	1.44	1.31
$R_{c,\alpha}$ (Å)	0.59	0.69	0.48	1.29

3.2. Amorphous $[Al]_{30}$ and $[Al]_{80}$

In the atomic structure calculations for the ternary amorphous $[Al]_x$ and $[Mg]_x$ ($x = 30$ and 80) alloys, we assumed the parameters associated with the d-electron contribution to Cu–Y, Y–Y, and Cu–Cu atomic pairs to be unchanged. Furthermore, we neglected the d-electron contribution to the atomic pairs M–Cu, M–Y, and M–M (M = Al or Mg), and hence used only the sp-electron contribution (2) as the interatomic potential [6]. Relevant parameters associated with the atomic pairs are listed also in table 1.
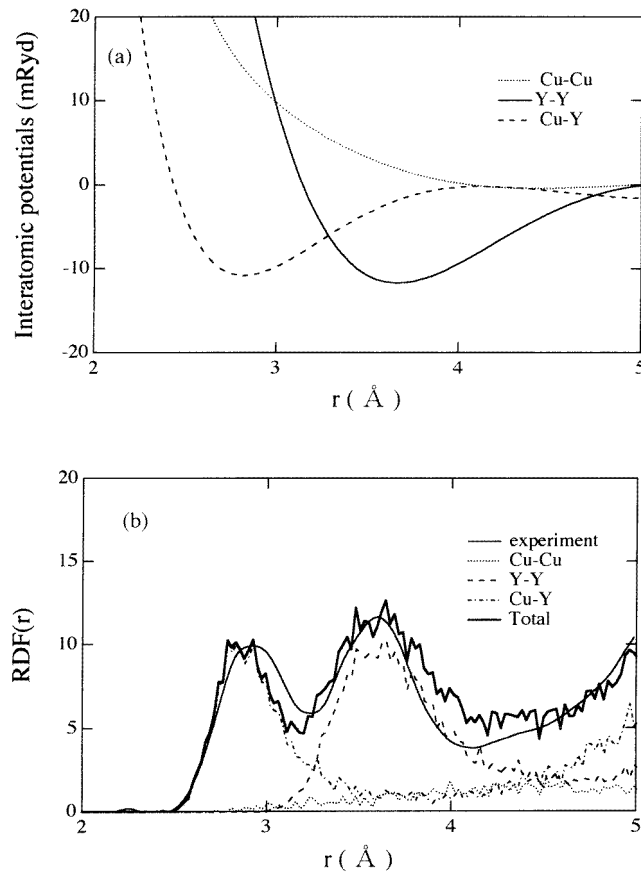
Figure 1. (a) Interatomic potentials associated with Cu–Cu, Y–Y, and Cu–Y atomic pairs in the amorphous $Cu_{40}Y_{60}$ alloy. (b) The RDF spectrum for the amorphous $Cu_{40}Y_{60}$ alloy in comparison with the measured RDF spectrum, reproduced from figure 4(a) in I.

It may be worth mentioning that, in the case of pure Al, only a shallow local minimum exists on the repulsive slope of the interatomic potential at the distance corresponding to the nearest-neighbour distance [7]. Because of the lower average sp-electron concentration in ternary [Al] alloys, the screening due to the sp electrons becomes less effective than that in pure Al and, in turn, the attractive bond energy contribution is reduced. This results in a shift of the minimum in the Al–Al potential to a larger distance and its deepening with decreasing Al concentration in the amorphous $[Al]_x$ alloys. In addition, it should be noted that the minimum in the Al–Cu potential for the $[Al]_{30}$ alloy is formed at the distance of 2.6 Å, which is much shorter than that of 3.2 Å in the Al–Al potential. This is essential to reproduce the local atomic structure observed in the amorphous $[Al]_{30}$ and $[Al]_{80}$ alloys.

The atomic structures for the amorphous $[Al]_x$ alloys with $x = 30$ and 80 were calculated, using the interatomic potentials thus derived. Since the hexagonal AlCuY and τ_2-phase intermetallic compounds exist near the compositions of the $x = 30$ and 80 alloys respectively as thermodynamically stable phases in the phase diagram, we employed them as starting structures. In total, 2000 atoms were employed. The resulting RDF spectra are shown in figure 2, onto which the measured RDF spectra from figure 5 in I are superimposed.

It can be seen that the calculated RDF spectra could reproduce well the measured ones in both amorphous alloys. The amorphous $[Al]_{30}$ alloy can be characterized by the atomic distributions such that the Al–Cu and Al–Y nearest-neighbour atomic pairs grow at the distance of 2.6 and 3.2 Å while the Cu–Y and Y–Y atomic pairs remain finite. Here it is also important to note that the distance of the Y–Y atomic pair is slightly expanded relative to that in the binary $Cu_{40}Y_{60}$ alloy. All these structural features are very consistent with the experimental results in I; the hybridization of the Al 3p states with Cu 3d and Y 4d states is stronger than that between Cu 3d and Y 3p states. It may be noted here that the p–d hybridization effect is not taken into account in the Hausleitner–Hafner approach described in equations (1)–(5), but we consider this effect to be in some sense included by intentionally displacing the minimum of the Al–Cu pair potential toward lower distances. This displacement is essential in the reproduction of the observed RDF structure and in avoiding the formation of Al–Al nearest-neighbour atomic pairs as evidenced from the observed RDF spectra.
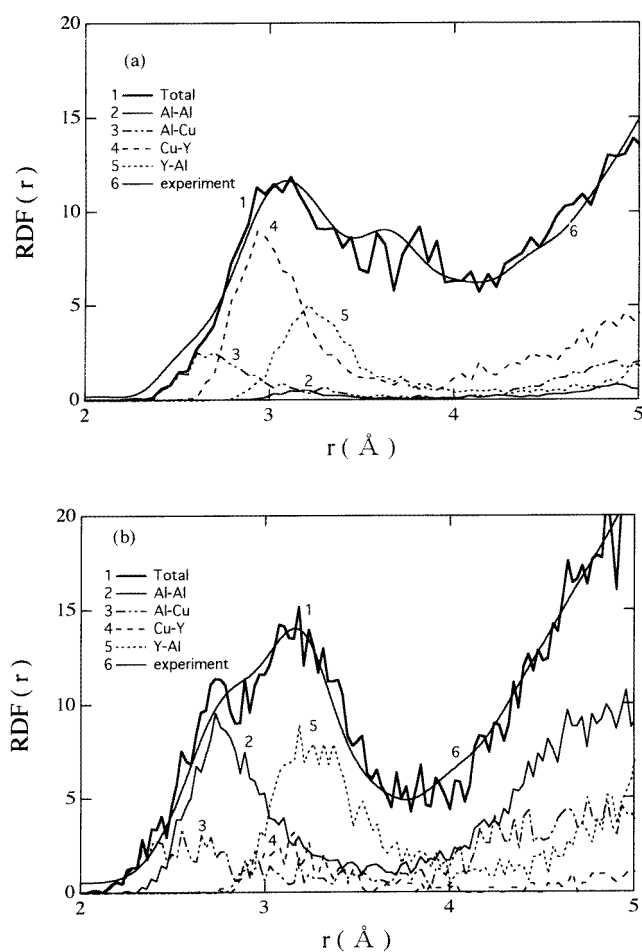

Figure 2. The calculated RDF spectra for the amorphous (a) $Al_{30}Cu_{28}Y_{42}$ and (b) $Al_{80}Cu_8Y_{12}$ alloys in comparison with the measured RDF spectrum reproduced from figure 5 in I.

Table 2. Radii of atomic spheres for the five amorphous alloys. Each average radius $r_{average}$ is determined so as to be compatible with that of the measured density in the respective amorphous alloys.

	$r_{average}$ (Å)	r_M (M = Al or Mg) (Å)	r_{Cu} (Å)	r_Y (Å)
$Cu_{40}Y_{60}$	1.73	—	1.67	1.76
$[Al]_{30}$	1.77	1.73	1.70	1.83
$[Al]_{80}$	1.62	1.60	1.55	1.76
$[Mg]_{30}$	1.75	1.74	1.68	1.79
$[Mg]_{80}$	1.79	1.79	1.66	1.84

The atomic structure of the amorphous $[Al]_{80}$ alloy is found to consist of the Al–Al nearest-neighbour atomic pair at the distance of 2.8 Å and the Al–Y atomic pair at 3.2 Å. A small contribution due to the Al–Cu atomic pair is also still visible at 2.6 Å. The atomic structure thus obtained for the $[Al]_{80}$ alloy is again well reconciled with the conclusion in I: each Cu and Y atom is fully surrounded by Al atoms and they exist as isolated impurities in the amorphous Al matrix.

3.3. Amorphous $[Mg]_{30}$ and $[Mg]_{80}$ alloys

We stressed that, in the case of $[Al]_{30}$ alloy, the Al–Cu atomic pair formed the minimum in the interatomic potential at the shortest atomic distance among all kinds of atomic pair. This is, indeed, crucially important for the formation of the Al–Cu correlation at the shortest distance in the resulting RDF spectrum. In contrast, the Cu–Y atomic pair possesses the shortest atomic distance among atomic pairs in the $[Mg]_{30}$ alloy. Hence, the Cu–Y atomic pair is expected to be preferentially formed in the amorphous [Mg] alloys.

The molecular dynamics calculation has been performed for both $[Mg]_{30}$ and $[Mg]_{80}$ alloys. Here a total of 2000 atoms are initially distributed over the liquid-like random lattice, since no intermetallic compounds exist near the compositions of these amorphous alloys. The calculated RDF spectra for the amorphous $[Mg]_{30}$ and $[Mg]_{80}$ alloys are shown in figure 3 together with the measured spectra reproduced from figure 4 in I. A good agreement with the observed spectra is obtained in both cases. The calculated spectra are characterized as follows: the Cu–Y and Y–Y atomic pairs remain finite without altering their positions while the Mg–Mg nearest-neighbour atomic pair has grown between them even in the $[Mg]_{30}$ alloy. This is in sharp contrast to the $[Al]_{30}$ alloy, where the formation of the Al–Al nearest-neighbour atomic pair was prohibited. It can be also seen in figure 3 that the Mg–Mg correlation dominates the spectrum when the Mg concentration reaches 80 at.%. All these features are very consistent with the conclusion drawn in I.

4. LMTO recursion band calculations for the amorphous alloys

The molecular dynamics modelling described above allows us to register the coordinates of all constituent elements for four ternary amorphous alloys plus the amorphous $Cu_{40}Y_{60}$ alloy in the computer. The space over which the atoms are distributed is divided into Voronoi polyhedra centred at each atom. Each polyhedron is formed by planes bisecting perpendicularly all nearest-neighbour distances around a given atom. An average volume of the Voronoi polyhedron is then calculated for a given atomic species by dividing the sum of volumes of all relevant polyhedra over its total number. The Voronoi polyhedron for
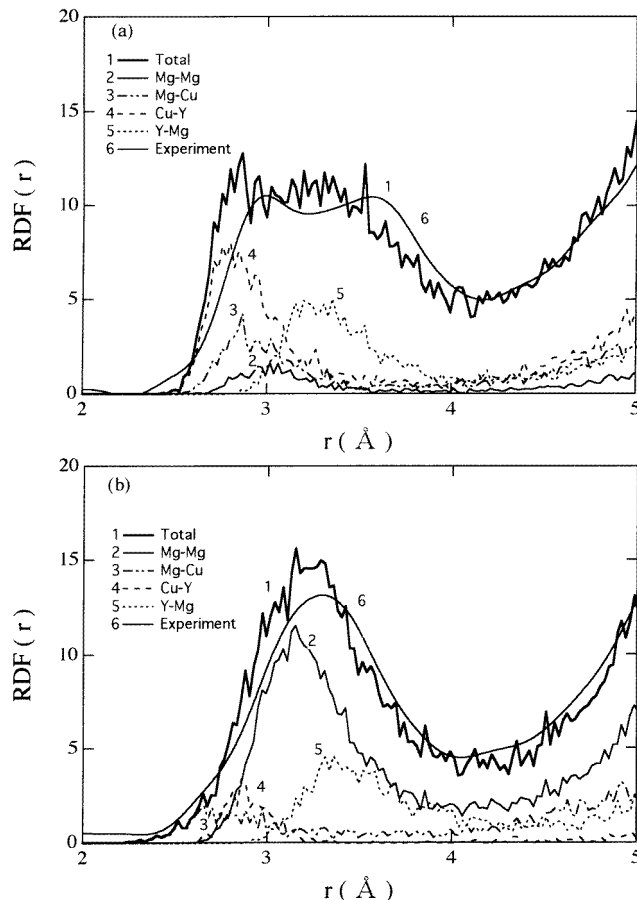
Figure 3. The calculated RDF spectra for the amorphous (a) $Mg_{30}Cu_{28}Y_{42}$ and (b) $Mg_{80}Cu_8Y_{12}$ alloys in comparison with the measured RDF spectrum reproduced from figure 4(b) and (c) in I.

each atomic species is replaced by an atomic sphere having the same volume. The radii of the atomic spheres of Al, Cu, and Y atoms thus obtained are listed in table 2.

The DOS for the amorphous alloys is calculated in the tight-binding LMTO scheme in combination with the recursion method. In this scheme, both the Hamiltonian matrix $H_{RL,R'L'}$ and overlap matrix $Q_{RL,R'L'}$ are expressed in real space, where R and L indicate the atomic position and a set of the azimuthal quantum number l and magnetic quantum number m, respectively [8,9]. The Hamiltonian and overlap matrices were calculated by choosing spherically 200 atoms around a given atom in the system consisting of a total of 2000 atoms. The 3s, 3p, and 3d states are taken into account as valence electrons in both the Al and Mg atoms, the 4s, 4p, and 3d states in the Cu atom, and the 5s, 5p, and 4d states in the Y atom. As a result, $1800(= 200 \times 9)$ different states appear and the 1800×1800 Hamiltonian and overlap matrix elements are obtained. The partial density of states is then calculated by the recursion method [10, 11]:

$$n_{Rl}(E) = -\pi^{-1}\mathrm{Im}\left\{\frac{1}{E + \mathrm{i}0 - a_1 - b_1^2/[E + \mathrm{i}0 - a_2 - b_2^2/(E + \cdots)]}\right\} \quad (6)$$

where a_n and b_n are the recursion coefficients in the range $1 \leqslant n \leqslant N$. We used here $N = 10$, 14, and 16 for the s, p, and d states, respectively. Because of the limited memory size in the present computer, we employed the squared-root terminator correction [12] for the d partial density of states to reduce the scatter of the DOS data points.

4.1. Electronic structure for the amorphous $[Al]_{30}$ and $[Al]_{80}$ alloys

Figure 4 shows the calculated Cu 3d and Y 4d partial density of states for the amorphous $[Al]_{30}$ and $[Al]_{80}$ alloys in comparison with that for the amorphous $Cu_{40}Y_{60}$ alloy. In the binary amorphous Cu–Y alloy, the Cu 3d band is found to be centred at the binding energy of 3.5 eV while the tail of the Y 4d states extend down to 5 eV. The whole spectrum is in good agreement with the measured XPS data and also that calculated by Hausleitner *et al* [5]. More important is the fact that we obtained an enhancement in the Y 4d states in the Cu 3d peak. This is taken as direct evidence for the occurrence of the hybridization effect between the Cu 3d and Y 4d states.
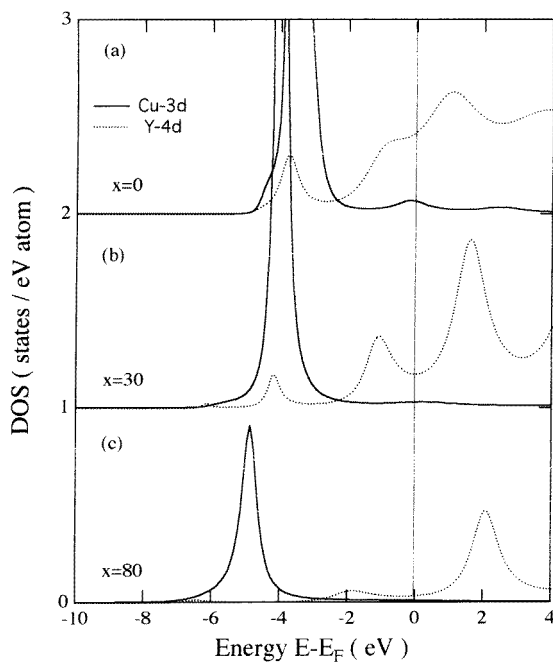

Figure 4. The calculated Cu 3d and Y 4d partial density of states for the amorphous (a) $Cu_{40}Y_{60}$, (b) $Al_{30}Cu_{28}Y_{42}$ and (c) $Al_{80}Cu_8Y_{12}$ alloys.

When Al atoms are added to the Cu–Y amorphous alloy, the Cu 3d peak shown in figure 4(b) and (c) is found to be displaced toward a higher binding energy in good agreement with the measured XPS spectra shown in figure 8 in I. This is taken as a clear indication of the weakening of the Cu 3d and Y 4d hybridization effect. In addition, we found that double peaks clearly appear at the binding energy of 1 eV and -1.5 eV in the $[Al]_{30}$ alloy. They can be attributed to the formation of the bonding and antibonding states due to the hybridization of Al 3p and Y 4d states. The Y 4d state is centred at 2 eV above the Fermi level in the $[Al]_{80}$ alloy. Indeed, the band widths of both Cu 3d and Y 4d states are found to be greatly reduced in the $[Al]_{80}$ alloy. This is very consistent with the structural

observation, which revealed the Cu and Y atoms as isolated impurities in the Al matrix. As a result of the strong interaction of the Al 3p states with the Y 4d states, the Cu 3d and Y 4d hybridization effect, significant in the binary Cu–Y alloy, is substantially weakened at $x = 30$ and diminished at $x = 80$.

The Al 3p partial densities of states for the amorphous $[Al]_x$ alloy with $x = 30$ and 80 are shown in figure 5. It reproduces well the observed Al $K\beta$ SXS spectra shown in figure 11 in I. We can, therefore, conclude from this calculation that the Al 3p states hybridize strongly with the Cu 3d and Y 4d states and, in turn, must be responsible for the suppression of the hybridization between the Cu 3d and Y 4d states. We could also confirm by calculations the recovery of the free-electron-like extended Al 3p states at $x = 80$.
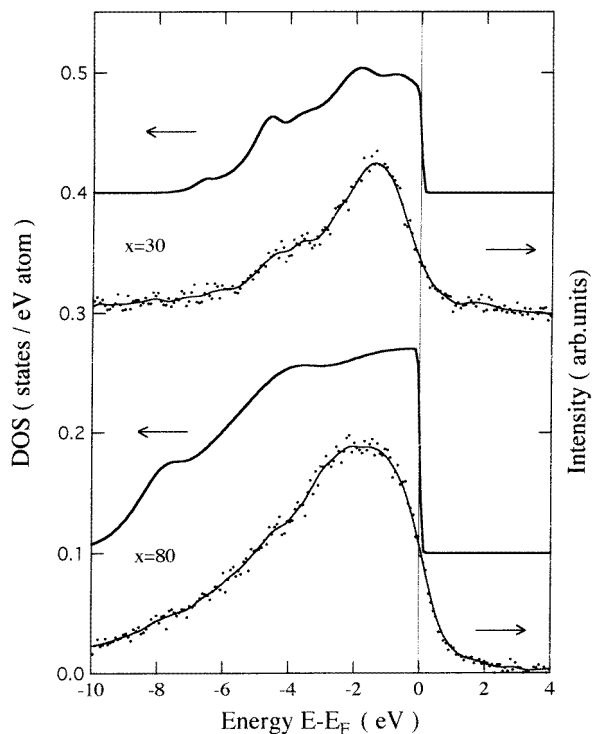

Figure 5. The calculated Al 3p partial densities of states for the amorphous $Al_{30}Cu_{28}Y_{42}$ ($x = 30$) and $Al_{80}Cu_8Y_{12}$ ($x = 80$) alloys. The Fermi–Dirac distribution function at $T = 300$ K is multiplied so that the state above the Fermi level is cut off. The data of Al $K\beta$ SXS spectra for the amorphous alloys are also shown in comparison (in arbitrary units).

4.2. Electronic structure for the amorphous $[Mg]_{30}$ and $[Mg]_{80}$ alloys

The Cu 3d and Y 4d partial densities of states for the amorphous $[Mg]_{30}$ and $[Mg]_{80}$ alloys are shown in figure 6, along with the data for the amorphous $Cu_{40}Y_{60}$ alloy. The displacement of the Cu 3d states with increasing Mg concentration is essentially absent and the hybridization effect between the Mg 3p and Y 4d states scarcely occurs, as opposed to the displacement of the Cu 3d states as well as the formation of the double peak across the Fermi level in the $[Al]_{30}$ alloy. Because of the weak interaction of the Mg 3p states with

the Cu 3d and Y 4d states, the Cu 3d and Y 4d hybridization effect remains substantial not only in the [Mg]$_{30}$ but also in the [Mg]$_{80}$ alloy. The Mg 3p partial densities of states are shown in figure 7 for the [Mg] alloys. It can be seen that the hybridization effect of the Mg 3p states with Cu 3d and Y 4d states is not as strong as that in the amorphous [Al] alloys.
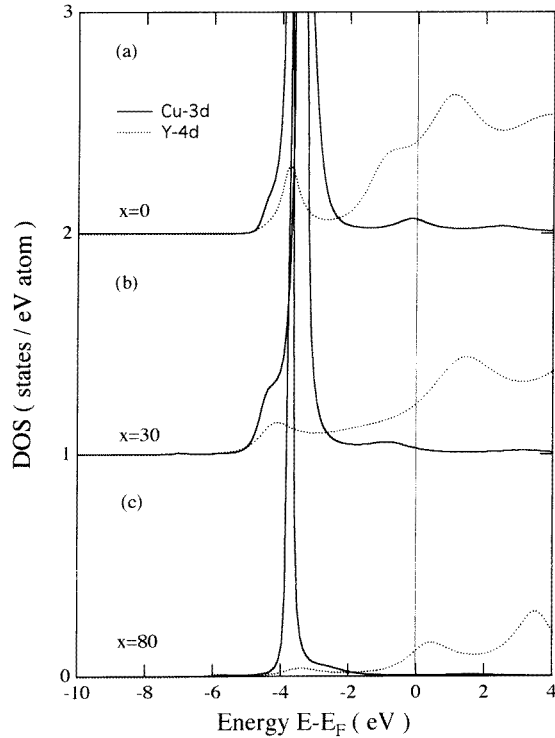

Figure 6. The calculated Cu 3d and Y 4d partial densities of states for the amorphous (b) Mg$_{30}$Cu$_{28}$Y$_{42}$ and (c) Mg$_{80}$Cu$_8$Y$_{12}$ alloys. (a) The data for the amorphous Cu$_{40}$Y$_{60}$ alloy are shown also in comparison.

Table 3. The Y 4d partial density of states at the Fermi level for the five amorphous alloys.

	Cu$_{40}$Y$_{60}$	[Al]$_{30}$	[Al]$_{80}$	[Mg]$_{30}$	[Mg]$_{80}$
DOS (states eV^{-1}/atom)	0.429	0.175	0.034	0.250	0.124

5. Interpretation of various physical properties

The crystallization temperature for the amorphous Cu$_{40}$Y$_{60}$ alloy was found in I to be 520 K. Its stability is owed to the strong bonding between the Cu 3d and Y 4d states, as revealed in the present study. The crystallization temperature further increases to 660 K in the [Al]$_{30}$ alloy, whereas it decreases to about 500 K for the [Mg]$_{30}$ alloy. It was shown that the amorphous [Al]$_{30}$ crystallizes into an almost single phase of the hexagonal
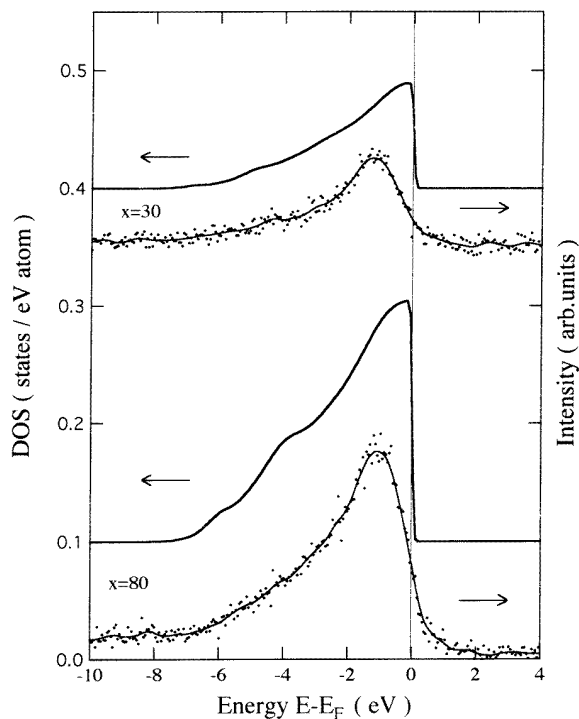
Figure 7. The calculated Mg 3p partial densities of states for the amorphous $Mg_{30}Cu_{28}Y_{42}$ ($x = 30$) and $Mg_{80}Cu_8Y_{12}$ ($x = 80$) alloys. The Fermi cut-off is introduced in the same way as in figure 5. The data of Mg Kβ SXS spectra for the amorphous alloys are shown also in comparison (in arbitrary units).

AlCuY intermetallic compound but the $[Mg]_{30}$ alloy is partitioned into a mixture of Mg-rich and Mg-poor phases [1]. The strong hybridization effect between the Al 3p and Y 4d states revealed in this study must be responsible for the enhancement in the crystallization temperature when Al atoms are introduced in the amorphous Cu–Y matrix. In contrast, the hybridization effect associated with Mg 3p states is weaker than that between the Cu 3d and Y 4d states but the amount of Cu–Y bonding is certainly reduced in proportion to the amount of Mg added to the amorphous Cu–Y matrix. This naturally explains a gradual decrease in the crystallization temperature in the amorphous [Mg] alloys.

We now discuss the Al and Mg concentration dependence of the electronic specific heat coefficient γ, which is known to be proportional to the density of states at the Fermi level. The density of states at the Fermi level is dominated by the Y 4d states in the present alloys. Hence, its value can be read off from figures 4 and 6. The result is listed also in table 3. It is clear that the value decreases much faster in the [Al] alloys than in the [Mg] alloys, in good agreement with the experimental data in I. The reason for this is now clear. The value of γ for the [Al] alloys is depressed due to the strong hybridization between the Y 4d and Al 3p states near the Fermi level. In contrast, the hybridization between Cu 3d and Y 4d states remains essentially unchanged when the Mg atoms are introduced and leaves more Y 4d states at the Fermi level than in the amorphous [Al] alloys. This is responsible for a substantial depression of the measured γ value for the $[Al]_{30}$ relative to that for the $[Mg]_{30}$ alloy shown in figure 16 in I.

Finally, we discuss the composition dependence of the electrical resistivity at 300 K for both [Al] and [Mg] alloys. The resistivity in the $[Al]_{30}$ alloy increases above the value of 210 $\mu\Omega$ cm for the amorphous $Cu_{40}Y_{60}$ alloy and becomes as high as 260 $\mu\Omega$ cm. In contrast, the value of resistivity for the amorphous $[Mg]_{30}$ alloy is reduced to about 180 $\mu\Omega$ cm. As has been emphasized in I, the mean free path of the conduction electrons at the Fermi level reaches an average atomic distance for all these high-resistivity amorphous alloys. Hence, the magnitude of the resistivity is expected to be almost inversely proportional to the density of states at the Fermi level and the Fermi velocity [13]. The formation of the strong hybridization of the Al 3p states with the Y 4d states contributes to reduce both the Fermi velocity and the number of electrons at the Fermi level. This must be responsible for the increase in the resistivity when the Al concentration is increased to 30–40 at.%. However, when the Al concentration reaches 80 at.%, we found that the Al 3p states resume more or less the free-electron-like band structure, as shown in figure 5. As a result, the resistivity value drops sharply when the Al–Al nearest-neighbours appear and its value increases above 60 at.% Al. Instead, the simple dilution effect dominates when the Mg atoms are introduced into the amorphous Cu–Y matrix, resulting in a linear decrease in resistivity with increasing Mg concentration.

As shown in I, the Hall coefficient is negative for the amorphous $Cu_{40}Y_{60}$ alloy. It becomes positive for the $[Al]_{30}$ alloy but remains negative for the [Mg] alloys. Therefore, the calculation of the Hall coefficient is of particular interest. We consider the emergence of a positive Hall coefficient to be deeply related to the unique electronic structure near the Fermi level in the $[Al]_{30}$ alloy. Further work is in progress along these lines.

Acknowledgments

References

[1] Fukunaga T, Sugiuru H, Takeichi N and Mizutani U 1996 *Phys. Rev.* B **54** 3200
[2] Fujiwara T 1984 *J. Non-Cryst. Solids* **61/62** 1039
[3] Andersen O K and Jepson O 1984 *Phys. Rev. Lett.* **53** 2571
[4] Heine V, Bullet D W and Haydock R 1980 *Solid State Physics* vol 35, ed H Ehrenleich, F Seitz and D Turnbull (New York: Academic) pp 1–294
[5] Hausleitner Ch, Tegze M and Hafner J 1992 *J. Phys.: Condens. Matter* **4** 9557
[6] Hausleitner Ch and Hafner J 1992 *Phys. Rev.* B **45** 115
[7] Hafner J 1987 *From Hamiltonian to Phase Diagrams* (Berlin: Springer)
[8] Andersen O K, Jepson O and Glötzel D 1985 *Highlight of Condensed Matter Theory* ed F Bassani, F Fumi and M P Tosi (New York: North-Holland)
[9] Nowak H, Andersen O K, Fujiwara T and Jepsen O 1991 *Phys. Rev.* B **44** 3577
[10] Nex C M M 1978 *J. Phys. A: Math. Gen.* **11** 653
[11] Haydock R and Nex C M M 1984 *J. Phys. C: Solid State Phys.* **17** 4783
[12] Haydock R and Nex C M M 1985 *J. Phys. C: Solid State Phys.* **18** 2235
[13] Mizutani U 1993 *Phys. Status Solidi* b **176** 9